

Quarterly Report for
Contract DE-FG36-08GO18192
Stanford Geothermal Program
January-March 2010

**Fracture Characterization in Enhanced Geothermal
Systems by Wellbore and Reservoir Analysis**

Table of Contents

1. FRACTURE CHARACTERIZATION USING PRODUCTION DATA	1
1.1 SUMMARY	1
1.2 INTRODUCTION	1
1.3 SIMPLIFIED DISCRETE FRACTURE NETWORK METHOD	3
1.4 FUTURE EXTENSIONS TO THE SIMPLIFIED DFN METHOD	12
1.8 CONCLUSIONS	15
2. FRACTURE CHARACTERIZATION OF ENHANCED GEOTHERMAL SYSTEMS USING NANOPARTICLES	17
2.1 SUMMARY	17
2.2 INTRODUCTION	17
2.3 SLIM TUBE EXPERIMENT	17
2.4 HEMATITE NANOFUID SYNTHESIS AND CHARACTERIZATION	24
2.5 FUTURE WORK	26
3. FRACTURE CHARACTERIZATION USING RESISTIVITY	27
3.1 SUMMARY	27
3.2 INTRODUCTION	27
3.3 RESISTIVITY MODELING	28
3.4 RESULTS	30
3.5 FUTURE WORK	34
4. REFERENCES	35

1. FRACTURE CHARACTERIZATION USING PRODUCTION DATA

This research project is being conducted by Research Assistant Egill Juliusson, Senior Research Engineer Kewen Li and Professor Roland Horne. The objective of this project is to investigate ways to characterize fractures in geothermal reservoirs using production data.

1.1 SUMMARY

In this quarterly report a fast and simple method for characterizing flow through a fracture network is discussed. The method is based on the assumption of steady-state, incompressible single-phase flow, which should be a relatively good approximation for most EGS (Enhanced Geothermal Systems) and other single-phase geothermal systems already in production. This method lends itself well to analysis by graph theory which has seen rapid development in the Computer Science industry in recent years (e.g. for analyzing road maps, internet searches, social networks etc.). Prototype algorithms to compute the fastest path, most transmissible path and largest flow path between wells were developed.

Nodal analysis of the fracture network led to a formulation which allowed explicit calculation of the flow rate along each fracture segment. Based on this information, the flow rate contribution was computed for each path connecting any two wells. This led to a method for analyzing the contribution of the fracture network to the dispersion seen in a tracer arrival profile. Being able to solve this problem without any numerical dispersion effects (which was one of the major goals stated in the last quarterly report) has brought us a step closer to characterizing the effects of fracture networks on production data.

Adding the effects of Taylor dispersion (molecular dispersion within each fracture) on tracer transport promises to be a feasible addition to the simulator. Adding thermal transport capabilities has been considered although that is expected to be more challenging. The simplified DFN method could also be used as a screening tool (proxy simulator) for Monte Carlo type history matching work flows.

1.2 INTRODUCTION

The Quarterly Report from Fall 2009 (Juliusson and Horne, 2009b) discussed a study of tracer and thermal transport through a discrete fracture network using a finite volume reservoir simulator similar to the well known TOUGH2 simulator. The discretization method used allowed explicit simulation of fractures with realistic dimensions. This also enabled us to easily visualize of the propagation of pressure, temperature and tracer saturation in the reservoir with time. The study gave some important insights into the differences between tracer and thermal transport through a fracture network. For example, the tracer response was shown to be more dependent on the specific fracture paths linking two wells than the thermal front. The reason for this was that the (nonreactive) tracer had negligible interaction with the matrix while the thermal front could only propagate when the fracture walls (adjacent matrix elements) had cooled down.

The downside of this full simulation method was that the rapid movement of the tracer front in the fractures caused the simulations to be very inefficient computationally and numerical dispersion was large and hard to quantify accurately.

In this report a fast but simplified numerical modeling method for calculating flow through a discrete fracture network is discussed. The method was developed based on the assumption of steady state, incompressible single-phase flow, which made the problem analogous to analyzing a network of resistors. The single-phase incompressibility assumption should be a relatively good approximation for most EGS (Enhanced Geothermal Systems) and other single-phase geothermal systems already in production. Assuming steady state flow should be valid if the purpose is to gain information about a fracture network based on a tracer test data, which for most practical purposes is obtained at steady-state flow conditions. Another advantage is that this method lends itself well to analysis by graph theory. Graph theory has seen rapid development in the Computer Science industry in recent years e.g. for analyzing road maps, internet searches, social networks etc.

The basic way the method works is to take an arbitrary network of fractures and break it down into a set of nodes (fracture intersections) and edges (fracture segments) that connect the nodes. The net inflow into each node is then used to set up a system of equations that describe the flow in the entire network. The system of equations can then be solved to find the flow rate in each fracture segment. At this point, some relatively efficient graph algorithms are employed to find all paths connecting any two wells. The travel time and flow rate attributable to each path can also be found, which means essentially that dispersion free tracer transport through the network has been found. Being able to solve this problem without any numerical dispersion effects (which was one of the major goals stated in the last quarterly report) has brought us a step closer to characterizing the effects of fracture networks on production data.

Adding the effects of Taylor dispersion (molecular dispersion within each fracture) on tracer transport promises to be a feasible addition to the method. Adding thermal transport capabilities will also be considered although that will be more challenging for two main reasons. First, thermal transport through the fracture network is known to be heavily dependent on interaction with the matrix. Secondly, the only viable analytical solution for thermal transport through fractures found from a brief literature survey has assumed infinite matrix boundaries, which effectively translates to zero fracture density. Modifying or deriving new or modified analytical solutions may be a challenging task.

Simplified models like these (referred to as proxy models) could be very useful for rapidly characterizing fracture network models. Such characterization would be particularly useful for history matching algorithms based on selecting a subset of a large number of stochastically generated models (Suzuki and Caers, 2008; Suzuki, Caumon, and Caers, 2008)

1.3 SIMPLIFIED DISCRETE FRACTURE NETWORK METHOD

In this section the development of a simplified method for characterizing fracture networks is described. The workflow involved creating a stochastic fracture network, simplifying that network into a set of connected nodes (fracture intersections) and edges (fracture segments), and computing the flow, travel time, transmissibility, etc., in each fracture segment. Finally the travel time, effective transmissibility and effective flow rate along every path was computed. A cross plot of each travel time versus the corresponding effective flow rate then lead to estimates analogous to the tracer arrival response, assuming no molecular dispersion.

1.3.1 Setting up the network graph

The first step in setting up the model was to generate a fracture network. A code for generating stochastic fracture networks was created using MATLAB. An example of one such network is shown in Figure 1.1. Each fracture was given a constant height (H), aperture (b) and permeability (k). In this particular instance the height was assumed to be constant but the aperture was assumed to be proportional to the fracture length and the permeability was assumed to be proportional to the square of the aperture (Takahashi et al., 1995; Watanabe and Takahashi, 1995).

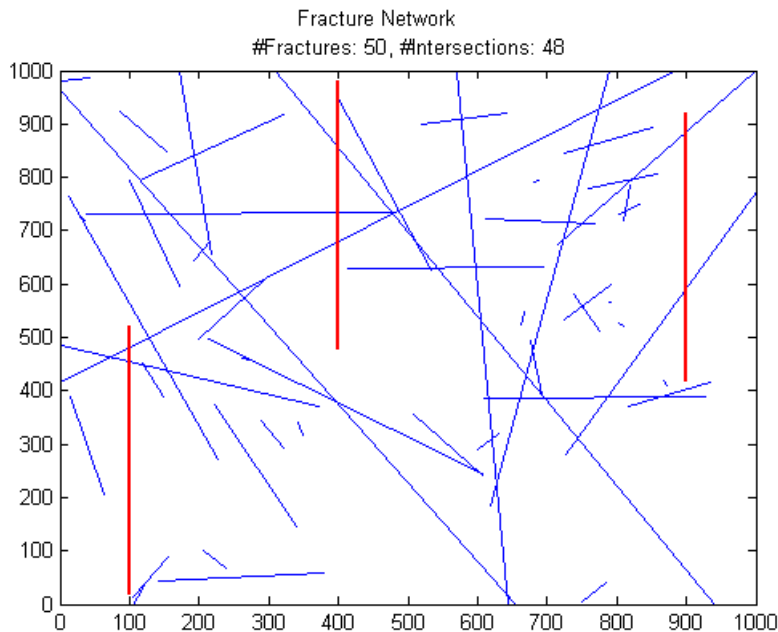


Figure 1.1: A two-dimensional stochastic fracture network with three wells. The fractures are the blue lines and the wells are the thicker red lines.

One of the main goals with the simplified method was to find the amount of flow in each path connecting any of the two wells and also to compute the time it would take to travel along each path. Note that two paths were defined as different if (and only if) they traversed one or more different fracture segments (edges) from point a to point b . Figure 1.1 illustrates clearly that some fractures did not connect any of the wells and could

therefore be eliminated from further analysis. This clean-up process was performed using a recursive graph traversal algorithm (depth first search). The standard way in which it was implemented is not optimal in terms of memory allocation, which limited the number of fractures that could be handled. Some improvement will be required at later stages; however, the algorithm worked quite well for a modest number of fractures (say 50). The results of the clean-up process are illustrated in Figure 1.2.

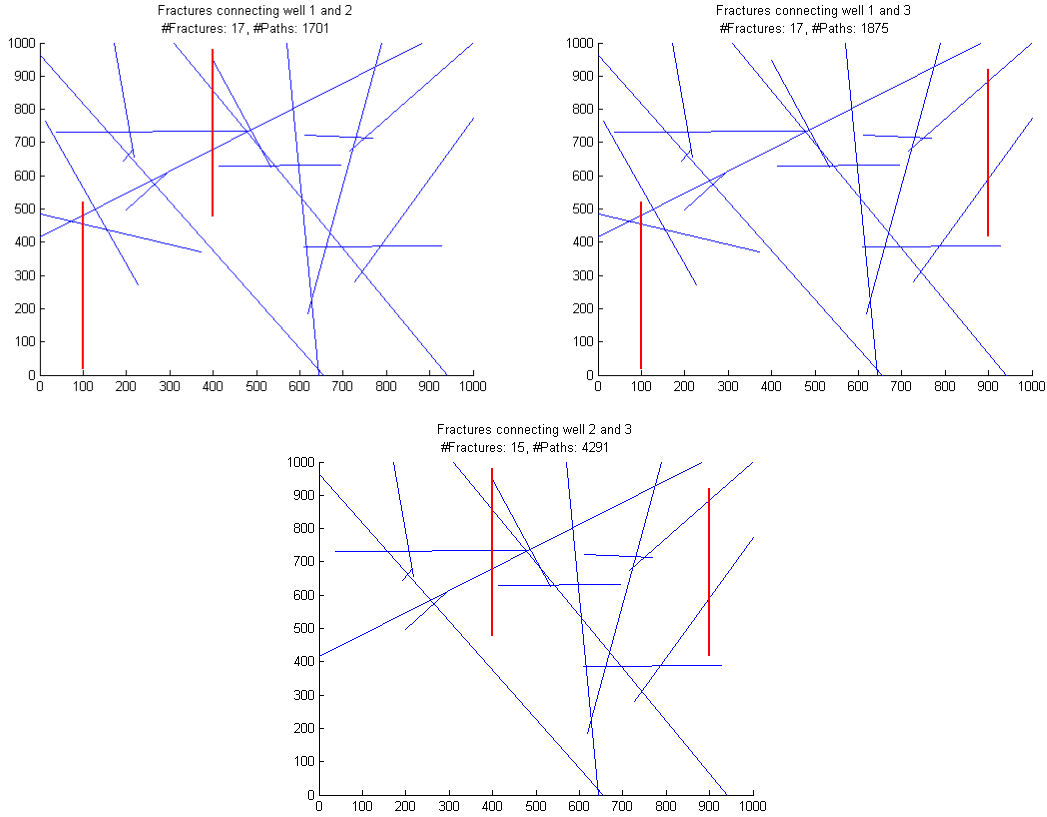


Figure 1.2: Remaining fractures on paths connecting each pair of wells. At this stage, all paths are assumed to be undirected, i.e. flow could go either way along each fracture segment.

Now each of the remaining fractures was broken into fracture segments (edges) and fracture intersections (nodes). An edge was only created for those fracture segments which would be on a path from one well to the other, so all fracture end segments were removed (Figure 1.3). Each fracture segment was given the same height, aperture and permeability as the corresponding fracture had. The length (L) was determined by the segment length. Then the segment transmissibility (T) was calculated from Equation (1.1).

$$T = \frac{kbH}{\mu L} \tag{1.1}$$

Here μ represents the dynamic viscosity of the fluid which was assumed to be constant at 10^{-3} Pa-s. The viscosity is generally not included in the transmissibility but it has been included in this case just to simplify the equations.

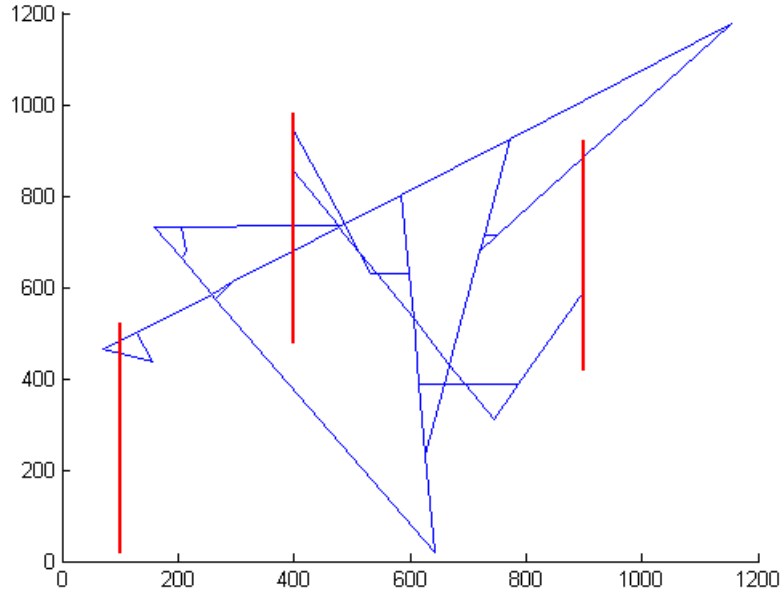


Figure 1.3: All fracture segments on connecting paths between well pairs.

1.3.2 Computing flow directions in the fracture network

After each of the nodes and edges had been defined the fracture system could be viewed as a resistor network and solved via nodal analysis. That is, given the assumption of incompressible, single-phase flow the net amount of flow into each node should sum up to zero. This led to a set of equations which could be set up in the following matrix form,

$$Jp = r \quad (1.2)$$

The elements of the matrix J were defined as

$$J_{ij} = \begin{cases} \sum_k T_k & \text{if } i = j \text{ and edge } k \text{ connects to node } i \\ T_k & \text{if } i \neq j \text{ and edge } k \text{ connects nodes } i \text{ and } j \\ 0 & \text{otherwise} \end{cases} \quad (1.3)$$

The vector p denoted the unknown nodal pressures and the right hand side vector was defined by Equation (1.4).

$$r_i = \begin{cases} \sum_k T_k p_j & \text{if edge } k \text{ connects node } i \text{ and known pressure node } j \\ 0 & \text{otherwise} \end{cases} \quad (1.4)$$

The known pressure nodes referred to in Equation (1.4) would be the (measured) pressure nodes where the fracture intersect the well.

Having solved for the pressure, the flow directions in each segment could easily be computed from Equation (1.5)

$$q_k = T_k (p_i - p_j) \quad (1.5)$$

where it is implied that fracture segment k connects nodes i and j . The flow velocity and travel time along each segment could also be calculated based on the area and length of the fracture segment. Figure 1.4 shows the flow direction computed along each of the fracture segments given a set of pressures in each well.

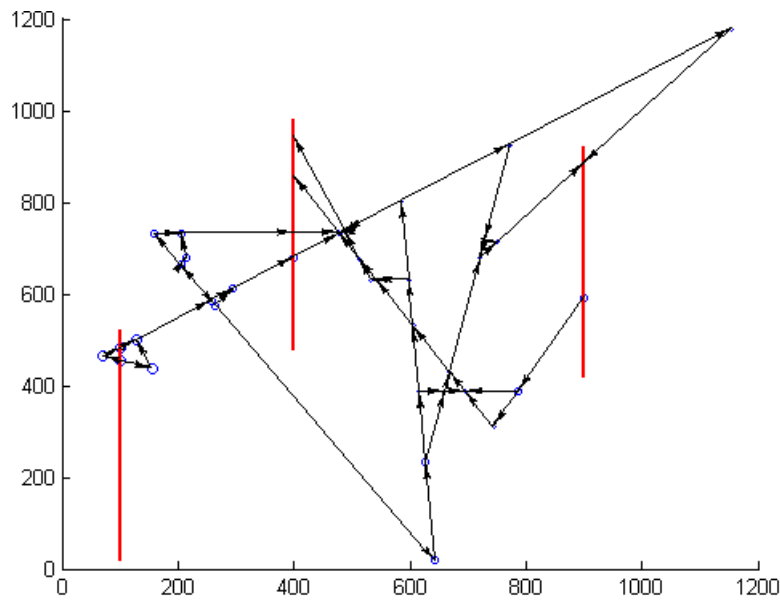


Figure 1.4: All directed paths in the fracture network for a given set of pressures in the wells. The black arrows show the flow direction. The sizes of the blue circles at each node represent the pressure.

Clearly, the flow patterns can become very complex. For example the fluid can move in opposite directions in different parts of the same fracture, and some paths will start and end in the same well. Table 1.1 summarizes the number of paths each well pair for the particular case illustrated in Figure 1.4.

Table 1.1: A summary of the number of paths connecting well pairs. The well numbers from 1 to 3 correspond to the order in which they are located in Figure 1.4, from left to right.

Start well \ End well	Well 1	Well 2	Well 3
Well 1	1	309	57
Well 2	0	2	0
Well 3	0	38	8

1.3.3 Path properties

To characterize the fracture network further, a number of path dependent properties were computed. Aside from the path length, the path travel time was perhaps the simplest to compute. Once the travel time in each fracture segment had been found (based on Eq. (1.5)), the total travel time along each path K , was computed as the sum of the travel times along each segment

$$t_K = \sum_k^N t_k \quad (1.6)$$

where k runs over each of the segments on path K .

The effective flow rate along each path, in other words the flow contribution attributable to each path connecting two points, was also of interest. The seemingly most straightforward way of computing this quantity was to propagate the proportion of flow going along each path as a weighted average of the flow exiting each node. The example network shown in Figure 1.5 will be used to illustrate this.

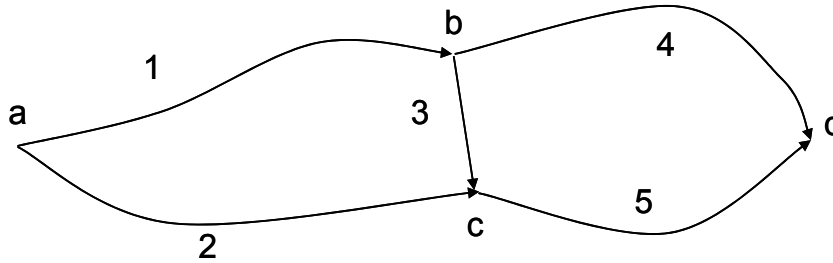


Figure 1.5: Fracture network used for an illustrative example. Nodes are labeled as a - d and edges 1-5. Arrows denote flow direction.

The flow rate in each segment could be found from Equation (1.5) (as shown by arrows). Three different paths lead from a to d , i.e. $\{1,4\}$, $\{1,3,5\}$ and $\{2,5\}$. At each node the stream is separated into one or more substreams, thus the flow rate (q) along each path could be computed as:

$$\begin{aligned}
q_{14} &= q_{tot} \frac{q_1}{q_1 + q_2} \frac{q_4}{q_3 + q_4} && \text{arrives at } t_1 + t_4 \\
q_{135} &= q_{tot} \frac{q_1}{q_1 + q_2} \frac{q_3}{q_3 + q_4} \frac{q_5}{q_5} && \text{arrives at } t_1 + t_3 + t_5 \\
q_{25} &= q_{tot} \frac{q_2}{q_1 + q_2} \frac{q_5}{q_5} && \text{arrives at } t_2 + t_5
\end{aligned} \tag{1.7}$$

Note that the sum of the three path streams equals $q_{tot}=q_1+q_2$. The general formulation is that the flow rate along each path, K , is

$$q_K = q_{tot} \prod_k \frac{q_k}{\sum_l q_l} \tag{1.8}$$

where k runs over all edges on path K , and l runs over all edges with outflow from the node which edge k has flow out of.

The effective transmissibility of each path, specific to the computed flow field, was computed as

$$T^*_K = \frac{q_K}{p_i - p_f} \tag{1.9}$$

where the subscripts i and f refer to the pressure at the initial and final node on path K .

Continuing the example shown in Figure 1.5 we could find each of the fastest, most transmissible and largest flow paths connecting any well pair. These are shown in Figure 1.6 along with each of the paths connecting well 1 to well 2, well 1 to well 3 and well 3 to well 2. Note that there were no connections in the reverse direction (e.g. from well 2 to well 1). Also, as noted in Table 1.1, each of the wells had a few paths leading back into the well itself.

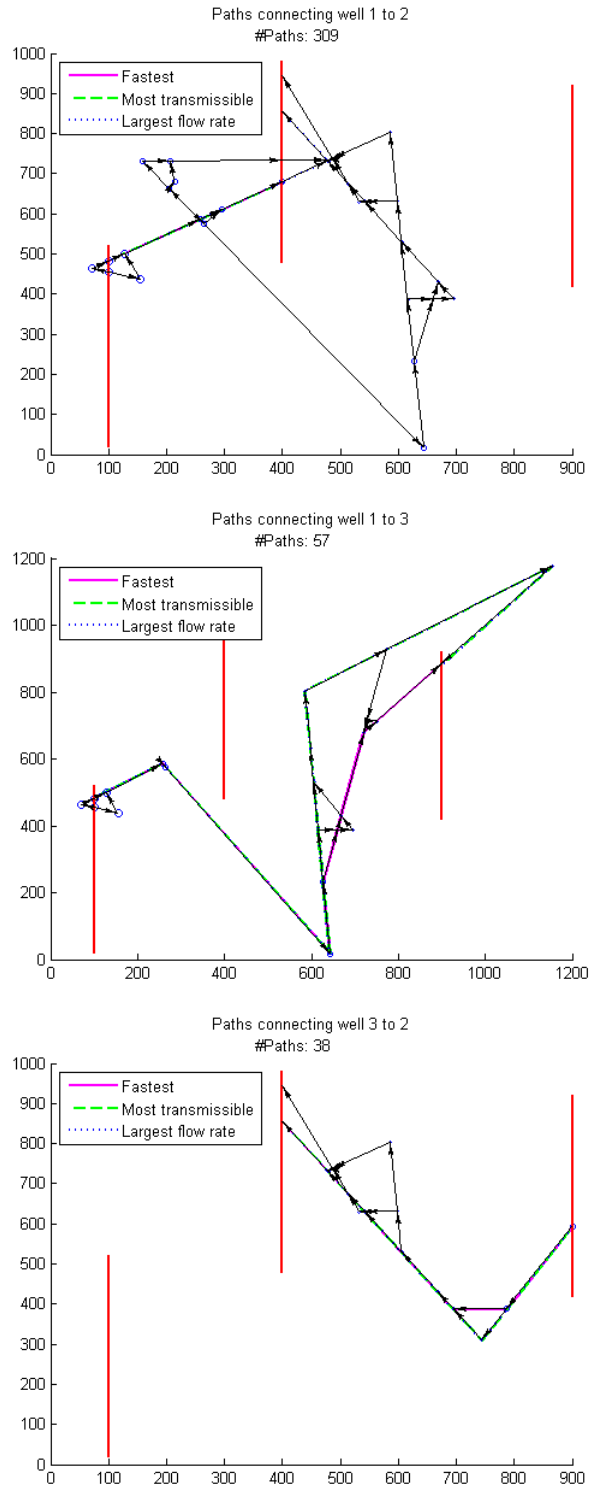


Figure 1.6: The ensemble of connecting paths for a few well pairs. Note that the fastest path, the most transmissible path and the path which carries the most flow are not necessarily the same.

A stem plot of the flow rate versus the arrival time along each path connecting wells 1 and 3 is shown in Figure 1.7. The figure also contains the cumulative flow rate vs. arrival time. The two plots are analogous to the impulse and step response to tracer injection if no dispersion were present. It is quite interesting to see that although there are over 50 paths connecting the two wells, only three of them carry any significant portion of the flow, and the travel times for these larger paths are relatively dispersed.

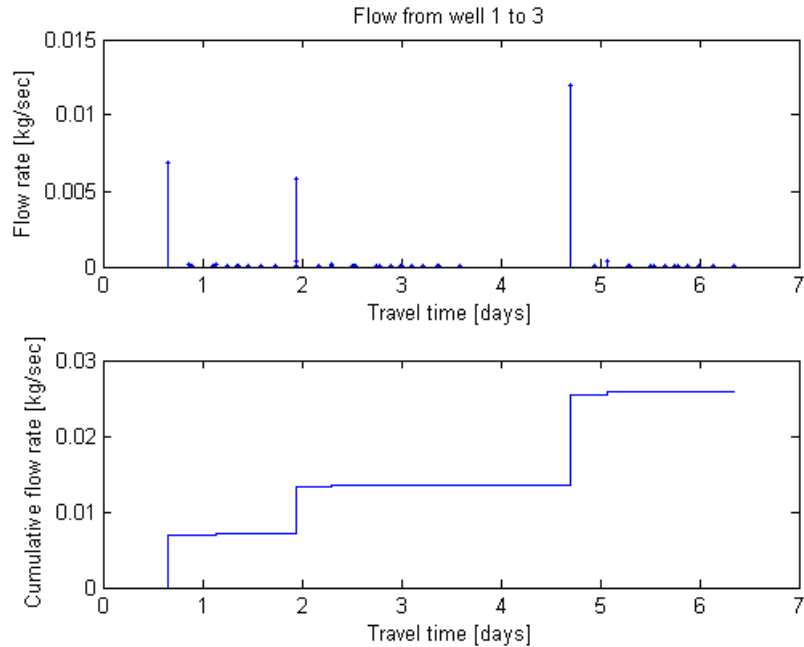


Figure 1.7: Flow rate vs. Travel time and Cumulative flow rate vs. Travel time for paths connecting well 1 to well 3.

A correspondence between large flow rates and small travel times was more commonly observed as was the case for flow from well 1 to well 2 (Figure 1.8) and from well 3 to well 2 (Figure 1.9). Notice also from the absolute values of the flow rates computed for each case, that by far the largest flow connection is between wells 1 and 2; this connection is mostly attributable to a single large fracture connecting the two wells.

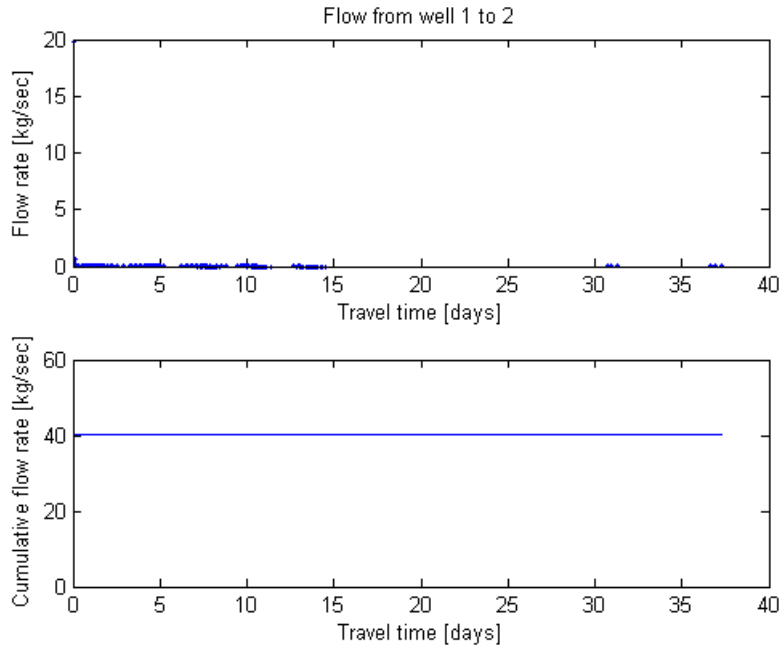


Figure 1.8: Flow rate vs. Travel time and Cumulative flow rate vs. Travel time for paths connecting well 1 to well 2.

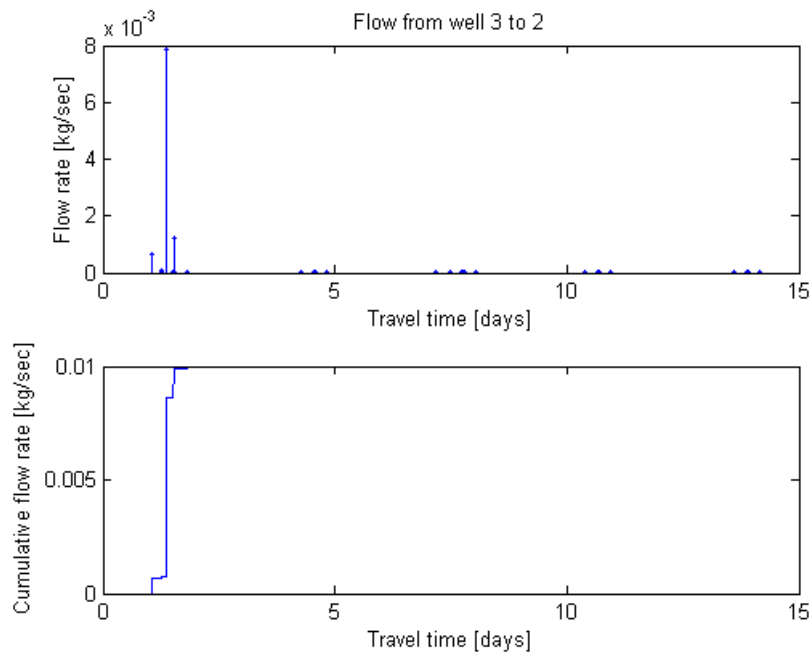


Figure 1.9: Flow rate vs. Travel time and Cumulative flow rate vs. Travel time for paths connecting well 3 to well 2.

1.4 FUTURE EXTENSIONS TO THE SIMPLIFIED DFN METHOD

Development of the simplified discrete fracture network (DFN) method is still at an early stage and a number of extensions have been conceived but not implemented yet. Following is a brief discussion of a few of these extensions.

1.4.1 Explicit path transmissibility

An alternative and perhaps a more rigorous approach to characterizing the transmissibility of paths in the fracture network would be first to find the effective transmissibility along each path without knowing the flow rate. To do this it is useful to note that transmissibility in a fracture network is analogous to conductivity (inverse of resistance) in a resistor network. In fact it can easily be derived that the effective transmissibility, T^* , through any number of fracture segments connected in parallel is equal to the sum of the transmissibilities of each fracture segment.

$$T^*_{parallel} = \sum_k T_k \quad (1.10)$$

Conversely, the effective transmissibility of any number of fracture segments connected in series is the harmonic sum of the transmissibilities of each fracture segment.

$$T^*_{series} = \left(\sum_k T_k^{-1} \right)^{-1} \quad (1.11)$$

These rules can be used to find the effective transmissibility of each path for simple fracture networks like the one shown in Figure 1.10. There are four different paths that can be taken from a to d , i.e. $\{1,3,4\}$, $\{1,3,5\}$, $\{2,3,4\}$ and $\{2,3,5\}$.

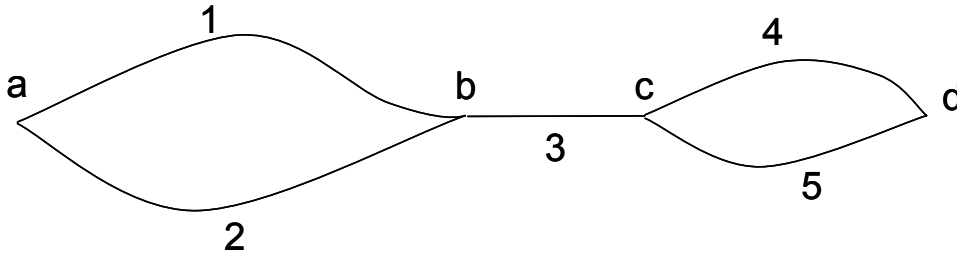


Figure 1.10: Simple fracture network used for illustrative purposes.

The effective transmissibility for the entire network follows from Equations (1.10) and (1.11):

$$\begin{aligned}
T_{ad}^* &= \left(T_{ab}^{*-1} + T_{bc}^{*-1} + T_{cd}^{*-1} \right)^{-1} \\
&= \left((T_1 + T_2)^{-1} + T_3^{-1} + (T_4 + T_5)^{-1} \right)^{-1} \\
&= \frac{T_1 T_3 T_4 + T_1 T_3 T_5 + T_2 T_3 T_4 + T_2 T_3 T_5}{T_1 T_3 + T_2 T_3 + T_1 T_4 + T_2 T_4 + T_3 T_4 + T_1 T_5 + T_2 T_5 + T_3 T_5}
\end{aligned} \tag{1.12}$$

This can be seen as a sum of four parallel paths where, for example, the transmissibility along path $\{1,3,4\}$ is:

$$T_{134}^* = \frac{T_1 T_3 T_4}{T_1 T_3 + T_2 T_3 + T_1 T_4 + T_2 T_4 + T_3 T_4 + T_1 T_5 + T_2 T_5 + T_3 T_5} \tag{1.13}$$

For more complicated networks however, Equations (1.10) and (1.11) will not suffice to reduce the network to a sum of parallel paths. An example of such a network would be the one shown in Figure 1.5 (neglect the directional arrows). To simplify this network the star-delta transform (discussed in Juliusson and Horne 2009b) needs to be used. Using the star-delta transform and some algebraic manipulation it can be show that the effective transmissibility of the fracture network in Figure 1.5 can be written as:

$$\begin{aligned}
T_{ad}^* &= \frac{T_1 T_4}{T_1 + T_4 + T_{23}^* + T_{35}^*} + \frac{T_1 T_{35}^*}{T_1 + T_4 + T_{23}^* + T_{35}^*} \\
&\quad + \frac{T_2 T_5}{T_2 + T_5 + T_{13}^* + T_{34}^*} + \frac{T_2 T_{34}^*}{T_2 + T_5 + T_{13}^* + T_{34}^*}
\end{aligned} \tag{1.14}$$

where T_{ij}^* denotes the star delta transform. The fracture network has effectively been broken into four parallel segments which go along each of the possible paths from a to d . A general formulation or algorithm for this type of reduction to a set of parallel paths has yet to be built, although it seems possible based on the two simple examples illustrated here. Doing that may be a particularly interesting way of viewing the fracture network, since such a characterization would be independent of the pressure distribution in the reservoir.

1.4.2 Taylor dispersion

One of the main incentives that brought us to work on the simplified DFN method was to find ways to compare the amount of dispersion caused by the fracture network itself with dispersion caused by molecular (and thermal) diffusion. As discussed in the Quarterly Report from Fall 2009, this type of comparison is not easily done using traditional finite volume reservoir models because of numerical dispersion effects. The DFN method is free of numerical dispersion. Moreover, it seems relatively simple to add Taylor dispersion effects to the model (at least for two dimensional models) using a semianalytical model.

The proposed method would be to use an analytical solution to the one dimensional advection-dispersion equation (Juliusson and Horne 2009a). The unit impulse kernel for this equation is defined as:

$$\kappa(x,t) = \frac{u}{2\sqrt{\pi Dt}} \exp\left[-\frac{(x-ut)^2}{4Dt}\right] \quad (1.15)$$

where L is the length of the fracture segment, u is the flow velocity and D is the dispersion coefficient. If an tracer slug of concentration c_o released at location $x=0$ over a (small) time interval Δt , the response seen at distance L_1 would be as described by Equation (1.16). This result can be computed by convolution.

$$c_1(L_1,t) = \int_0^t c_o \Delta t \delta(t-\tau) \kappa_1(\tau) d\tau = \frac{c_o \Delta t u_1}{2\sqrt{\pi D_1 t}} \exp\left[-\frac{(L_1 - u_1 t)^2}{4D_1 t}\right] \quad (1.16)$$

Here the subscript 1 refers to the properties of fracture segment 1 (edge 1, linking nodes 1 and 2). Similarly, the response at the next node (node 3, which we assume to be linked to node 2 via edge 2) could be computed by the convolution of $c_1(t)$ and the unit impulse kernel for edge 2.

$$c_2(L_2,t) = \int_0^t c_1(L_1, t-\tau) \kappa_2(\tau) d\tau \quad (1.17)$$

Considering the fact that node 2 could branch out to more than one edge (say edges 3 and 4) the response at node 3 could be computed as:

$$c_2(L_2,t) = \frac{q_2}{q_2 + q_3 + q_4} \int_0^t c_1(L_1, t-\tau) \kappa_2(\tau) d\tau \quad (1.18)$$

Continuing in this manner all the way to the final node would give the effective dispersive response along each path. Taylor dispersion would be modeled by using Equation (1.19) to compute the dispersion coefficient in each fracture segment (Horne and Rodriguez 1983).

$$D_{Taylor} \approx \frac{2}{105} \frac{u^2 b^2}{D_{mol}} \quad (1.19)$$

The molecular diffusion coefficient, D_{mol} , should be on the order of 10^{-10} m²/s.

1.4.3 Thermal dispersion

Adding thermal dispersion effects to the simple DFN method seems to be a bit more challenging than adding tracer dispersion effects. The main reason for this is that the propagation of the thermal front depends much more strongly on the matrix surrounding the fractures and to some extent the interaction between the various flow paths through the

matrix. An analytical solution (Lauwerier 1955) has been identified which can be used to describe the propagation of a thermal front in a planar fracture surrounded by two infinite slabs of impermeable rock. The equation is as follows

$$T_n(x,t) = \frac{T_o - T(x,t)}{T_o - T_{inj}} = \operatorname{erfc} \left\{ \left[\frac{(\rho_w C_w)^2 \left(\frac{qH}{Ax} \right)^2 \left(t - \frac{\phi \rho_w C_w + (1-\phi) \rho_r C_r}{\rho_w C_w} \frac{Ax}{q} \right) \right]^{-1/2} \right\} \quad (1.20)$$

where now T denotes the temperature, ρ is density, C is specific heat capacity, K is thermal conductivity, ϕ is porosity and A is the cross sectional area of the fracture (normal to the flow direction). The subscript o refers to the initial state, r refers to the rock and w to the water.

Equation (1.20) should work well when only one major flow path dominates the flow in the reservoir or if the major flow paths are few and far apart. If however, there are multiple large flow paths cooling down the reservoir at similar time scales, these flow paths will interact with each other through the matrix. To account for that, it might be possible to derive an equation similar to Eq. (1.20), but with less restrictive boundary conditions (e.g. with surrounding rock matrix slabs of finite dimension, or even a specific shape). This would presumably make it easier to implement semi-analytical approximations to what the thermal arrival profile might look like, even when there are several major flow paths interacting through the matrix.

1.4.4 Characterizing and screening an ensemble of DFNs

The simple DFN method is in a way a proxy model for discrete fracture networks. Proxy models are commonly employed when an approximate, quick solution is sought, e.g. in history matching work flows (Suzuki, Caumon, and Caers, 2008; Suzuki and Caers, 2008). The tracer response for a given set of well pressures can be quickly approximated using the simple DFN method. Therefore, if tracer data is available, the method should be a good screening tool for accepting or rejecting plausible models from an ensemble of stochastically generated DFNs.

The applicability of doing this type of screening could be tested by generating an ensemble of fracture networks and taking one of those as the “true” reservoir. The tracer response of each of the other models would then be computed and compared to the “true” model response with some sort of acceptance criterion. Thereafter, the ensemble of accepted fracture networks would be compared to the initial ensemble created to get a sense of how much the tracer history match reduced the uncertainty in the fracture distribution. The “true” model could also be used to compute the tracer response at another set of well pressures. The new set of pressures would then be used for all the other models created and the range of uncertainty about the tracer response (and thermal response) could be compared using the entire initial ensemble, and the history matched ensemble.

1.8 CONCLUSIONS

A method for characterizing discrete fracture networks was conceived and a prototype algorithm illustrating some of the basic capabilities of the method was built. The method is

based on an assumption of steady state, incompressible, single-phase flow, which allowed the flow through the network to be analyzed in a manner analogous the finding current in a resistor network. These assumptions should be relatively good for analyzing liquid dominated geothermal fields, at steady state flow conditions. The algorithm works quite fast, and of the coding is based on graph theory, a branch of computer science which has seen significant advances in recent years.

The method was shown to be capable of quantifying the dispersion of flow attributable to the fracture network. The method is free of numerical dispersion effects, but numerical dispersion was the main attribute interfering with our previous analysis of tracer and thermal breakthrough curves in fracture networks using traditional finite volume reservoir simulators (Juliussen and Horne, 2009b).

Further extensions to and applications of the method are planned. A way of incorporating Taylor dispersion effects on tracer flow has been suggested. Some thought has also been given to the incorporation of thermal dispersion effects, although this part will require a bit more development. Finally, we have identified the applicability of using this method as a proxy simulator for Monte Carlo based history matching algorithms with discrete fracture network models.

2. FRACTURE CHARACTERIZATION OF ENHANCED GEOTHERMAL SYSTEMS USING NANOPARTICLES

This research project is being conducted by Research Associates Mohammed Alaskar and Morgan Ames, Senior Research Engineer Kewen Li and Professor Roland Horne. The objective of this study is to develop in-situ multifunction nanosensors for the characterization of Enhanced Geothermal Systems (EGS).

2.1 SUMMARY

The slim tube experiment was initiated to test the feasibility of passing nanoparticles through longer pore networks than have previously been tested. The injected nanoparticles were transported 10 meters through the sand-packed slim tube and were detected in the effluent. Scanning Electron Microscopy (SEM) imaging demonstrated unambiguously that the nanoparticles had been transported through the pore spaces within the sand-packed tube. Hematite (Fe_2O_3) nanoparticles, informally called “nanorice” due to their spindle shape, were synthesized to continue to investigate the transport of nonspherical particles through porous media.

This report describes the results of the silicon dioxide nanoparticle injection into the 10 meter sand-packed slim tube, as well as the synthesis and characterization of the hematite sample.

2.2 INTRODUCTION

Last quarter’s report (October-December 2009) described the motivation of the slim tube experiment, the construction of the slim tubes, the calibration of transducers, and the details involving the permeability and porosity measurements and calculations. During the current quarter, the slim tube experiment was performed and analyzed. This included the characterization of the injected nanofluid as well as effluent samples. To further investigate the transport of nonspherical particles through porous media and to gain experience in the synthesis of nanomaterials, a hematite (Fe_2O_3) nanofluid sample was synthesized and characterized using Electron Microscopy.

2.3 SLIM TUBE EXPERIMENT

This section provides the results of the first injection of the nanofluid (SiO_2) into a thin sand-packed plastic tube (Figure 2.1). The details of the standard measurements of porosity, permeability and pore volume calculations of the slim tube can be found in the last quarterly report (October-December 2009). The porosity of the sand was measured by resaturation with pure water and found to be around 35% with pore volume in the order of 52 milliliters. The liquid permeability was found to be approximately 50 darcy.

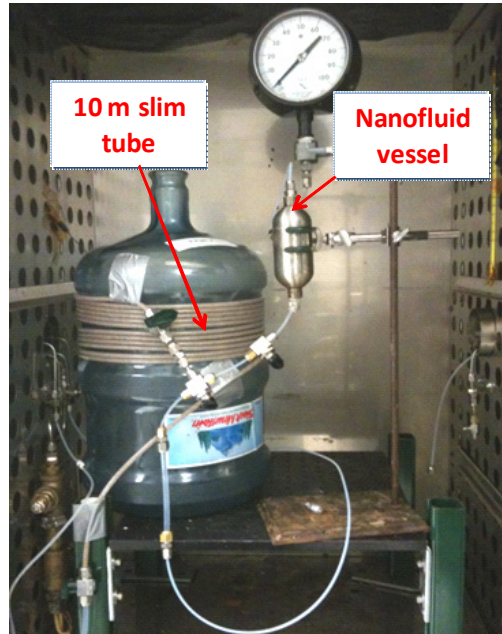


Figure 2.1: Polypropylene 10 meter slim tube.

The objective of this experiment is to investigate the transport and recovery of nanoparticles through a longer flow path approaching actual field distances such as in interwell tracer testing. The silicon dioxide nanoparticles were detected at the effluent, confirming their transport (Figure 2.2). The permeability was unaltered during and after the injection of the nanofluid with minimal change of about ± 4 darcy. This can be seen in a plot of the permeability as function of pore volumes injected (Figure 2.3). Notice the high frequency of measurement points at the beginning of the post injection of pure water to capture any change in concentration of nanoparticles as more water was injected.

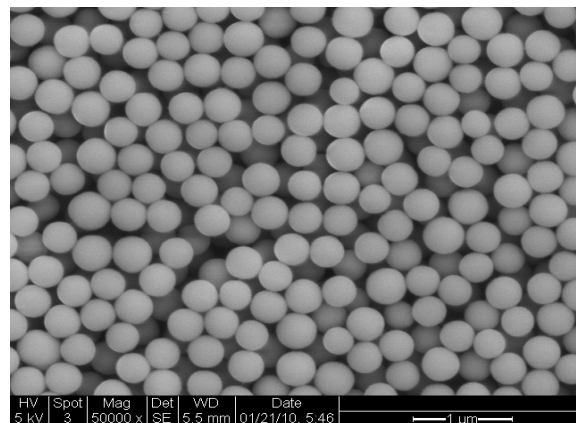


Figure 2.2: Effluent sample containing SiO_2 nanoparticles.

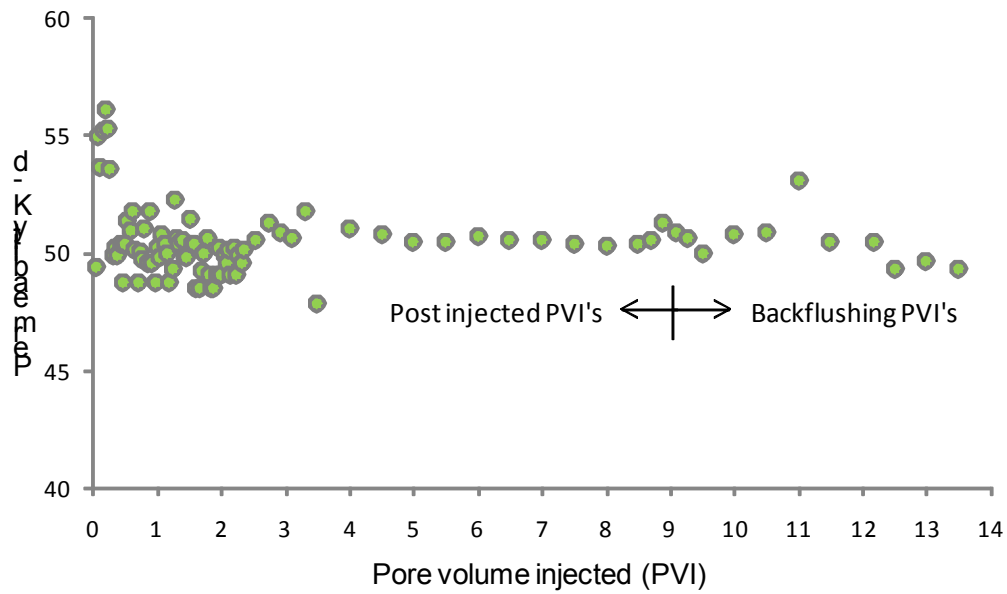


Figure 2.3: Permeability measurements during, after as well as during backflushing of the slim tube.

The SiO₂ nanoparticles injected had an average particle size of approximately 350 nanometers as demonstrated in Figures 2.4 and 2.5 by light scattering and scanning electron microscopy, respectively.

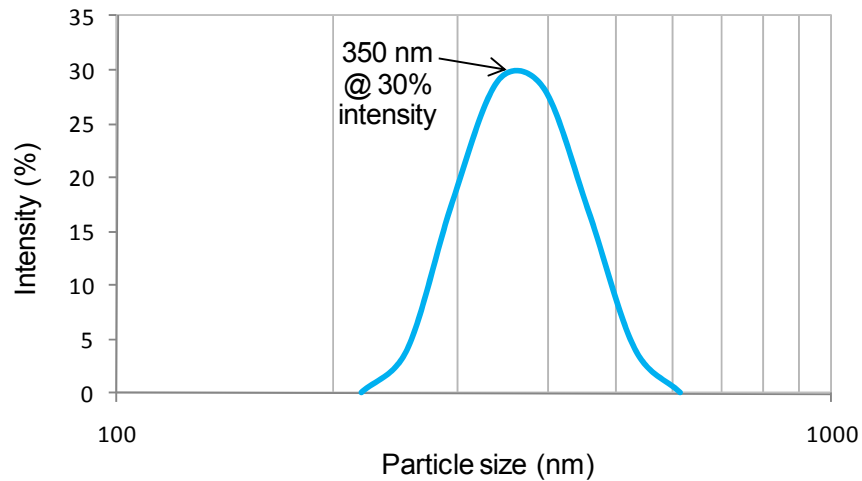


Figure 2.4: Particle size distribution by light intensity percentage of the influent injected.

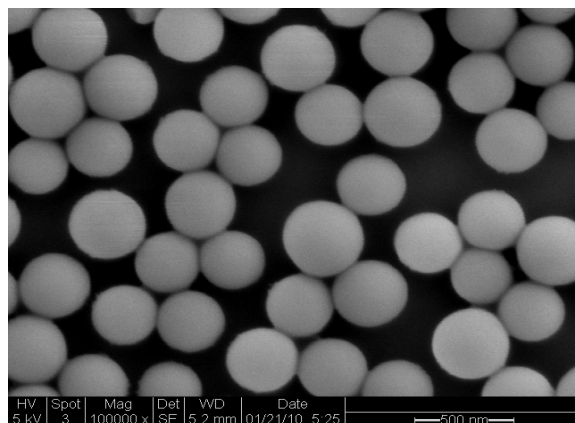


Figure 2.5: Monodisperse SiO₂ nanospheres of the influent with an average size of 350 nm.

Based on the light scattering measurements, the intensity of the incident light should remain unchanged for every particle size regardless of the sample concentration. In this case, the intensity of around 30% was measured at particle size of 350 nanometers of the original nanofluid injected (Figure 2.4). Therefore, effluent samples collected during post injection of pure water that contain any nanoparticle concentrations within the detection limits of the instrument used should have the same intensity for that particular particle size. The light intensity of effluent samples is plotted against post injected pore volumes (PVI) in Figure 2.6.

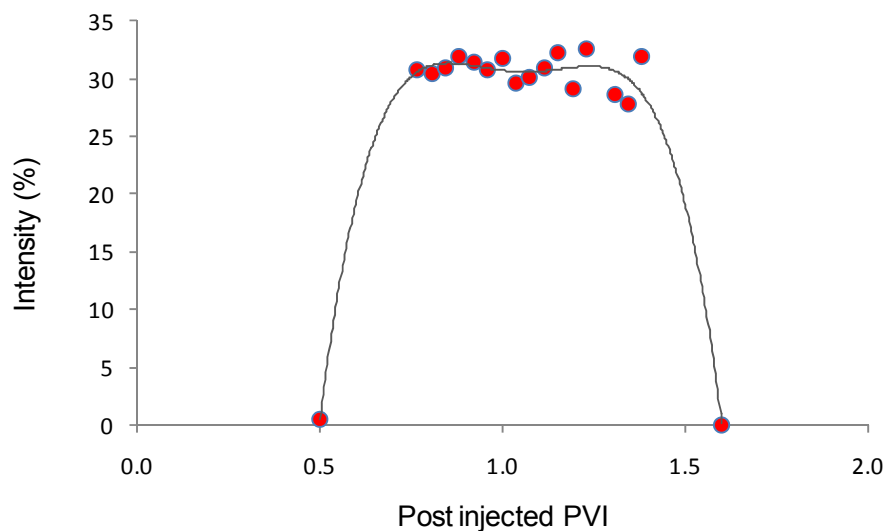


Figure 2.6: Intensity measurements of effluent samples.

It is evident from Figure 2.6 that the nanoparticles exist in the effluent samples with same intensity of the original silicon dioxide nanofluid influent (i.e. 30%) as depicted in Figure 2.4. The nanoparticles were identified following the post injection of about half of one

pore volume of pure water and produced continuously until the bulk of these particles were displaced through the second pore volume. The increasing content of nanoparticles within that pore volume can be observed visually, as shown in Figure 2.7. Cloudy samples are more highly concentrated with SiO₂ nanoparticles compared to more transparent samples.

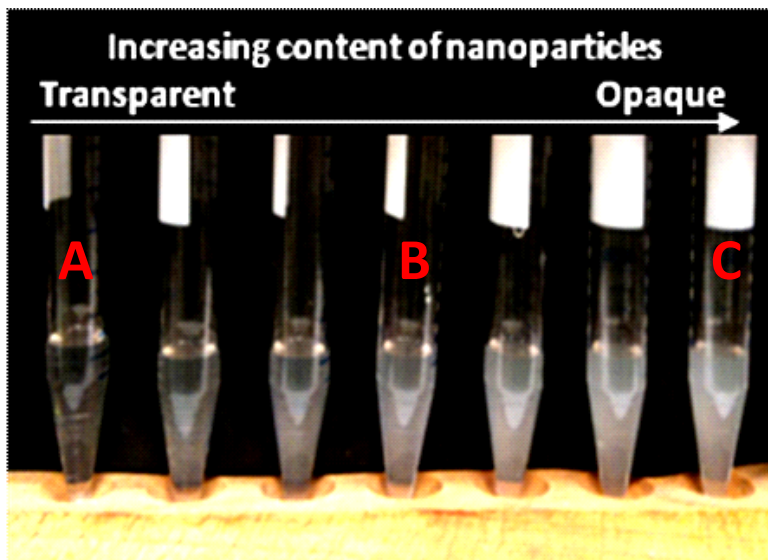


Figure 2.7: Visual characterization of effluent samples for their SiO₂ nanoparticles content based on color.

Scanning electron imaging has confirmed the variation in the particle concentrations. A series of SEM images (Figure 2.8) were taken for samples A, B and C of Figure 2.7. These images show the difference in particle count or concentration clearly. Note that the volume of each sample was identical and micrographs were taken at the same magnification.

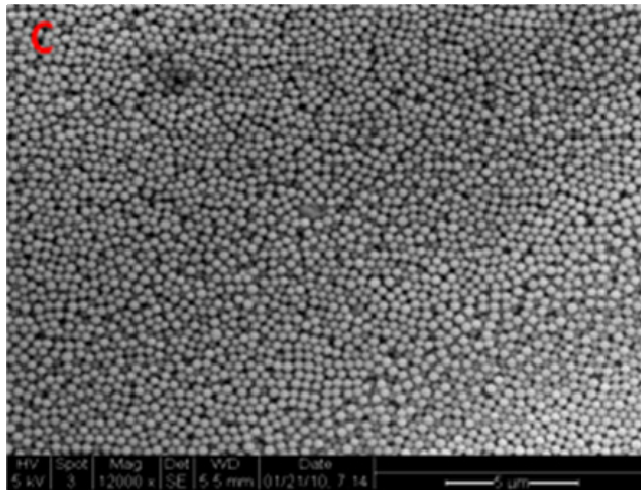
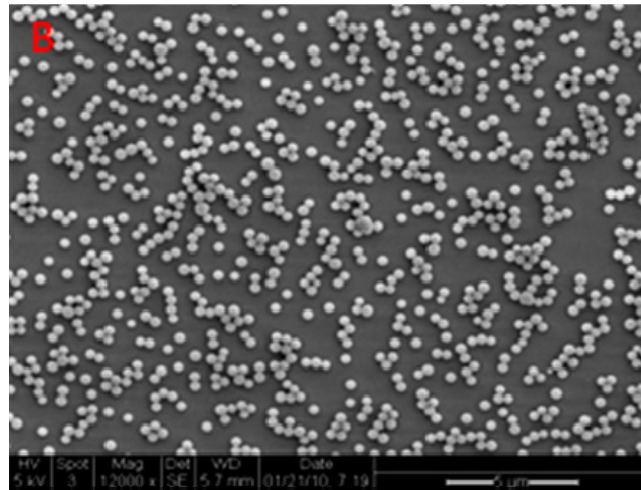
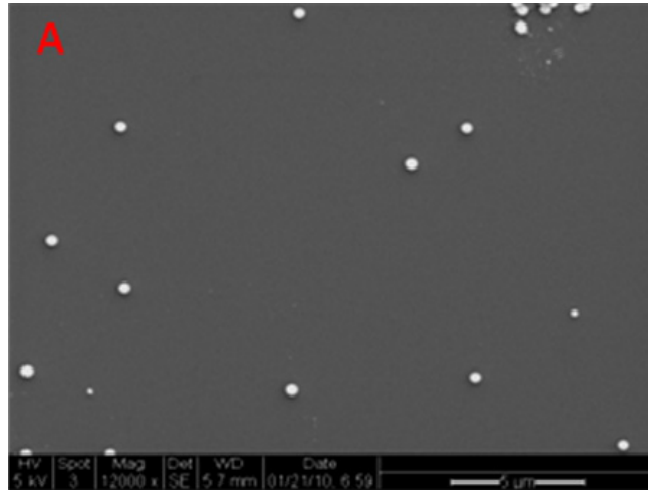


Figure 2.8: SEM images at sample A, B and C of Figure 2.7.

It is worth mentioning that not all SiO₂ nanoparticles were recovered following the second pore volume injected. A method to measure nanoparticle concentration has not been identified at this time. However, scanning electron imaging of selective samples within later pore volumes produced can indicate if they still exist. For instance, an effluent sample at the middle of the third post injected pore volume contained traces of the silicon dioxide nanoparticles, as opposed to another sample at the eighth pore volume, which was found to be free of any nanoparticles (Figure 2.9).

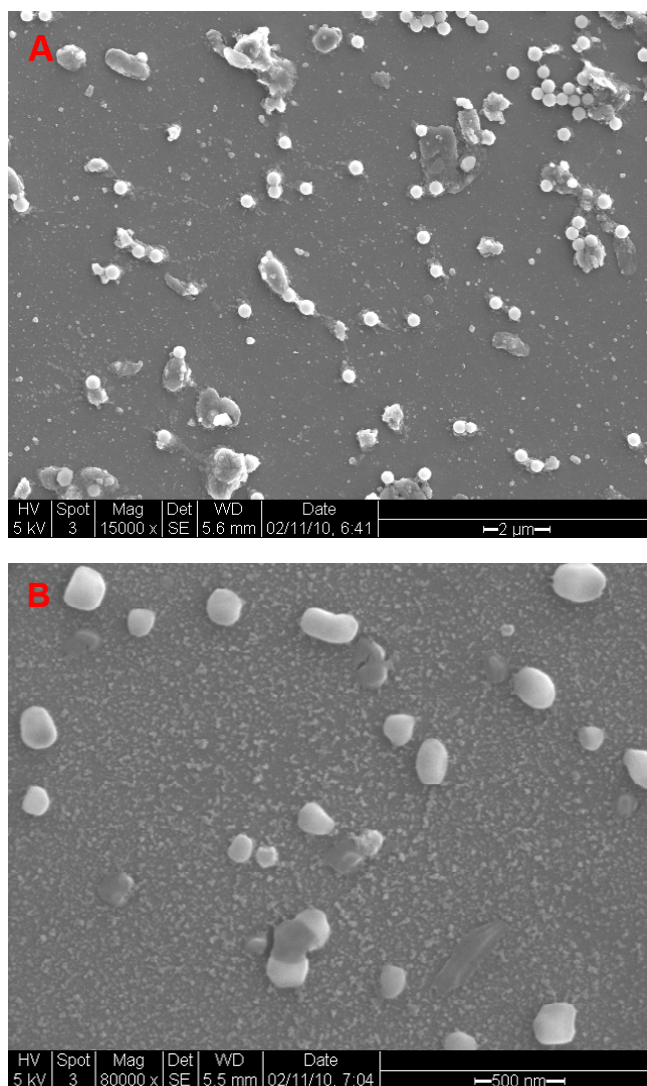


Figure 2.9: SEM image of effluent sample at the (A) third and (B) eighth post injected pore volumes.

It was realized that this finding did not imply the full recovery of all injected particles (but at least the mobile ones). The sand-packed slim tube was backflushed with few pore volumes in an attempt to determine whether there were any trapped nanoparticles, especially at the inlet side. An SEM image of the effluent from the first backflushed pore

volume is shown in Figure 2.10, where the spherical silicon dioxide nanoparticles can be seen clearly. Later backflushed pore volumes have not been analyzed yet.

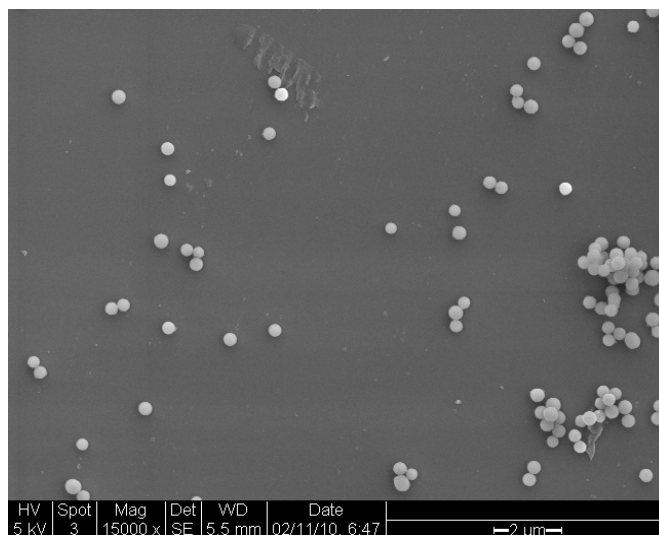


Figure 2.10: SEM image of effluent sample at the first backflushed pore volume.

Thus, it has been demonstrated that the spherically-shaped nanoparticles can be recovered following their injection, not only through short core plugs, but also through a longer flow path. In the experiments, the nanoparticles were transported without being trapped within the flow conduits. The details of the silicon dioxide injection into a core can be found in a previous quarterly report (April-June 2009).

2.4 HEMATITE NANOFLUID SYNTHESIS AND CHARACTERIZATION

Hematite (Fe_2O_3) nanoparticles were synthesized and characterized using Scanning Electron Microscopy. Hematite was chosen for a number of reasons. First, it furthers the investigation of the feasibility of transporting nonspherical nanoparticles through porous media, which began with silver nanowire experiments reported in the July-September 2009 quarterly report (the silver nanowires were not transported successfully, but were trapped at the inlet of the core). The relatively simple synthesis process involved in making hematite nanoparticles also served as a valuable introduction to nanoparticle synthesis. Further, the surface chemistry of these nanoparticles can be modified, and there are known processes for coating hematite nanorice with other nanomaterials, which makes it a valuable candidate for temperature-sensitive applications (Connor, 2010). Hematite is also stable at reservoir conditions, and can be easily detected by its optical and magnetic signals. Finally, due to its unique rice-shaped geometry, it can be distinguished visually from natural minerals that may be present (using Electron Microscopy).

Monodisperse hematite nanoparticles were synthesized using forced hydrolysis of solutions of ferric chloride, as suggested by Ozaki (1984). This hydrothermal synthesis was carried out by preparing 100 ml of aqueous solution of 2.0×10^{-2} M FeCl_3 and $4.0 \times$

10^{-4} M KH_2PO_4 and holding it at 100°C for 72 hours (Wang, 2006). The precipitated nanoparticles were centrifuged and washed several times, then dispersed in 100 ml of water. These nanoparticles were found to be roughly 500 nm in length and 100 nm in diameter, resulting in an aspect ratio of 5:1 (Figures 2.11, 2.12).

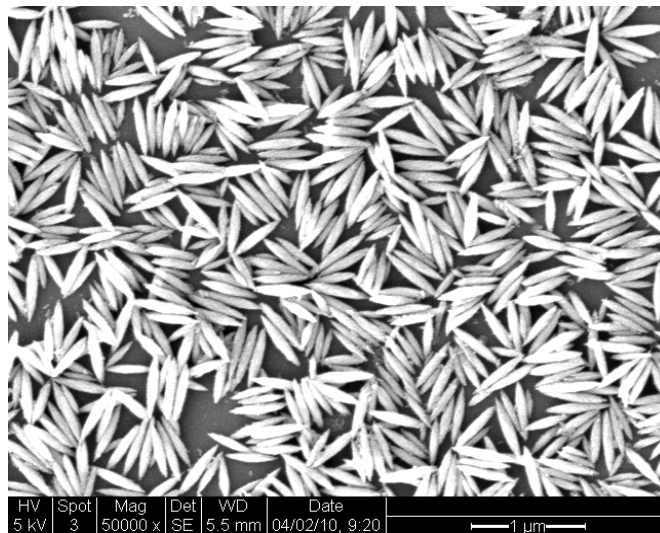


Figure 2.11: SEM image of hematite nanoparticles

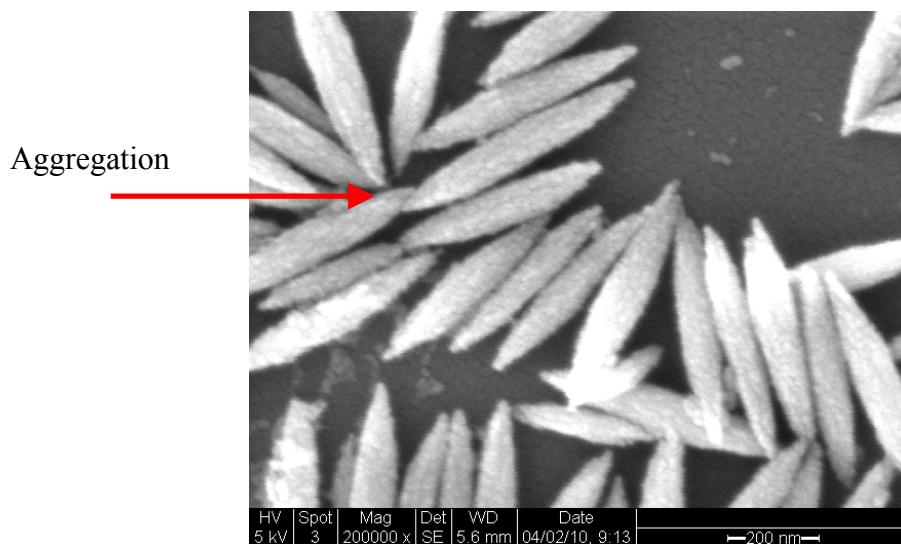


Figure 2.12: SEM image of hematite nanoparticles at higher magnification

As can be observed in Figures 2.11 and 2.12, the anisotropic hematite particles have a tendency to aggregate in clusters. This phenomenon can be explained by the Gibbs-Thomson effect. Essentially, the aggregation occurs to reduce the free energy of the anisotropic particles. The change in free energy due to aggregation can be approximated by the change in chemical potential due to size or curvature, which in turn can be attributed to a change in the free energy at the surfaces (Equation 2.1).

$$\Delta\mu = \frac{2 * \gamma * \Omega_A}{R} \quad (2.1)$$

$\Delta\mu$ is the change in chemical potential, γ is the surface tension, Ω_A is the atomic volume, and R is the radius of curvature.

Since nonspherical particles are anisotropic with respect to curvature, they are also anisotropic with respect to chemical potential, which is highest where the radius is smallest. Thus, nonspherical particles are more prone to aggregation than spherical ones with isotropic curvature. Furthermore, the aggregation can be expected to occur at high frequency where the radius of curvature is small in order to cover parts of the surface with high free energy. This can be observed in Figures 2.11 and 2.12. This aggregation could potentially cause problems in transport through pore networks.

2.5 FUTURE WORK

The next stage will be to determine the concentration of nanoparticles in effluent samples. This is of particular importance because it enables us to investigate their recovery and study the particle flow mechanism. Knowing the nanoparticles concentration will allow for the construction of the tracer return curve or production history which then can be compared to that for conventional (chemical) tracer.

The injection of hematite nanorice is also planned. The objective of this experiment is to investigate the feasibility of recovering nonspherical nanoparticles through porous media. The testing of this idea began with the injection of silver nanowires, the details of which can be found in a previous quarterly report (July-September 2009). The silver nanowires were found trapped at the inlet of the sandstone core. Note that they had a longitudinal dimension in range of 5-10 micrometers. It has been hypothesized that their geometry may have imposed constraint on their transport through the core. To verify this hypothesis, a trial injection of the shorter hematite nanorice (less than 1 micron) will be conducted. Berea sandstone and sand-packed slim tubes will be used in this injection. As a preliminary test, injection into a glass bead packed tube will also be carried out to investigate the interactions between the hematite and the glass beads, which can be used to model the pore network in real core rock.

3. FRACTURE CHARACTERIZATION USING RESISTIVITY

This research project is being conducted by Research Assistant Lilja Magnusdottir, Senior Research Engineer Kewen Li and Professor Roland Horne. The objective of this project is to investigate ways to use resistivity to infer fracture properties in geothermal reservoirs.

3.1 SUMMARY

The aim of this part of the project is to use resistivity measurements and modeling to characterize fracture properties in geothermal fields. The resistivity distribution in the field can be estimated by measuring potential differences between various points and the resistivity data can be used to infer fracture properties due to the large contrast in resistivity between water and rock.

A two-dimensional model has been made to calculate a potential field due to point sources of excitation. The model takes into account heterogeneity by solving the potential field for inhomogeneous resistivity. Fractures are modeled as areas with resistivity different from the rock, to investigate the changes in the potential field around them. In the second phase of the project, which this report mainly discusses, the model is used to investigate the possibility of using potential difference between only two points in a reservoir to infer at what angle a straight fracture, between the points, is aligned. Various fracture patterns are also examined in order to study the correspondence between potential differences and fracture patterns.

Future work will involve investigating further the possibility of using the model to characterize fracture patterns in two dimensions from potential distribution. Ways to enhance the contrast between fracture and rock resistivity will also be explored to ease the fracture characterization. Different resistivity measurements and modeling techniques will be explored as well.

3.2 INTRODUCTION

The designing of optimal production wells in geothermal reservoirs requires knowledge of the resource's connectivity and heat intensity for energy extraction. Drilling and construction of wells are expensive and the energy content from a well depends highly on the fractures it intersects. Fracture characterization is therefore important to increase the reliability of geothermal wells and thereby the overall productivity of geothermal power plants.

In this project, the goal is to find ways to use Electrical Resistivity Tomography (ERT) to characterize fractures in geothermal reservoirs. ERT is a technique for imaging the resistivity of a subsurface from electrical measurements. Typically, electrical current is injected into the subsurface through conducting electrodes and the resulting electrical potentials are measured. Due to the large contrast in resistivity between water and rock, the resistivity measurements could be efficiently used to indicate fracture locations.

Resistivity measurements have been widely used in the medical industry to image the internal conductivity of the human body, for example to monitor epilepsy, strokes and lung functions as discussed by Holder (2005). In Iceland, electrical resistivity tomography

methods have been used to map geothermal reservoirs. Arnarson (2001) describes how different resistivity measurements have been efficiently used there to locate high temperature fields by using electrodes located on the ground's surface. Stacey et al. (2006) investigated the feasibility of using resistivity to measure geothermal core saturation. A direct current pulse was applied through electrodes attached in rings around a sandstone core and it resulted in data that could be used to infer the resistivity distribution and thereby the saturation distribution in the core. It was also concluded by Wang (2000) that resistivity data has high resolution power in depth direction and is capable of sensing the areal heterogeneity.

In the approach considered in this project, electrodes would be placed inside geothermal wells and the resistivity anomalies studied between them to locate fractures and infer their properties by resistivity modeling. Due to the sparsity of measurement points, i.e. limited number of test wells, we will endeavor to find ways to improve the process of characterizing fractures from limited resistivity data. To enhance the contrast in resistivity between the rock and fracture zones, the possibility of using conductive fluid will be explored. Furthermore, the influences of temperatures and fluid stream on resistivity measurements will be studied. The effects of mineralization in the fractures will also be examined, as fractures containing minerals may be easier (or more difficult) to distinguish from the surrounding rocks. This report first describes the resistivity model that has been made to calculate a potential field due to point sources of excitation and then discusses the attempt to use that model to characterize different fractures patterns.

3.3 RESISTIVITY MODELING

One of the main problems in resistivity modeling is to solve the Poisson's equation that describes the potential field and to efficiently complete the inversion iteration. That governing equation can be derived from some basic electrical relationships as described by Dey and Morrison (1979). Ohm's Law defines the relationship between current density, J , conductivity of the medium, σ , and the electric field, E , as

$$J = \sigma E \quad (3.1)$$

The stationary electric fields are conservative, so the electric field at a point is equal to the negative gradient of the electric potential there, i.e.

$$E = -\nabla \phi \quad (3.2)$$

where ϕ is the scalar field representing the electric potential at the given point. Hence,

$$J = -\sigma \nabla \phi \quad (3.3)$$

Current density is the movement of charge density, so according to the continuity equation, the divergence of the current density is equal to the rate of change of charge density,

$$\nabla J = \frac{\partial Q(x, y, z)}{\partial t} = q(x, y, z) \quad (3.4)$$

where q is the current density in amp m⁻³. Combining Equations (3.3) and (3.4) gives the following Poisson's equation which describes the potential distribution due to a point source of excitation,

$$\nabla[\sigma \nabla \phi] = -q(x, y, z) \quad (3.5)$$

The conductivity σ is in mhos m^{-1} and the electric potential is in volts. This partial differential equation can then be solved numerically for the resistivity problem.

3.3.1 Finite Difference Equations in Two Dimensions

The finite difference method was used to approximate the solution to the partial differential Equation (3.5) using a point-discretization of the subsurface (Mufti, 1976). The computational domain is discretized into $N_x \times N_y$ blocks and the distance between two adjacent points on each block is h , as shown in Figure 3.1.

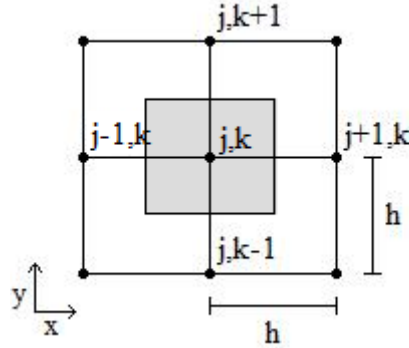


Figure 3.1: Computational domain, discretized into blocks.

Taylor series expansion is used to approximate the derivatives of Equation (3.5) about a point (j, k) on the grid,

$$\left. \frac{\partial}{\partial x} \left(\sigma \frac{\partial \phi}{\partial x} \right) \right|_{(j,k)} \approx \frac{\left[\begin{array}{l} \phi(j+1,k)\sigma\left(j+\frac{1}{2},k\right) + \phi(j-1,k)\sigma\left(j-\frac{1}{2},k\right) \\ - \left[\sigma\left(j+\frac{1}{2},k\right)\sigma\left(j-\frac{1}{2},k\right) \right] \phi(j,k) \end{array} \right]}{h^2} \quad (3.6)$$

$$\left. \frac{\partial}{\partial y} \left(\sigma \frac{\partial \phi}{\partial y} \right) \right|_{(j,k)} \approx \frac{\left[\begin{array}{l} \phi(j,k+1)\sigma\left(j,k+\frac{1}{2}\right) + \phi(j,k-1)\sigma\left(j,k-\frac{1}{2}\right) \\ - \left[\sigma\left(j,k+\frac{1}{2}\right)\sigma\left(j,k-\frac{1}{2}\right) \right] \phi(j,k) \end{array} \right]}{h^2} \quad (3.7)$$

The point (j, k) represents the shaded area in Figure 3.1 (area = h^2) so the current density due to an electrode at that point is given by,

$$q(j,k) = I / h^2 \quad (3.8)$$

where I [amp] is the current injected at point (j, k) Combining Equations (3.5)-(3.8) and solving for the electric potential ϕ at point (j, k) gives,

$$\phi(j,k) = \frac{[I + \phi(j+1,k)c_1 + \phi(j-1,k)c_2 + \phi(j,k+1)c_3 + \phi(j,k-1)c_4]}{c_1 + c_2 + c_3 + c_4} \quad (3.9)$$

The parameters c_i represent the conductivity averaged between two adjacent blocks, i.e.

$$c_1 = \frac{2}{\rho(j,k) + \rho(j+1,k)} \quad (3.10)$$

$$c_2 = \frac{2}{\rho(j,k) + \rho(j-1,k)} \quad (3.11)$$

$$c_3 = \frac{2}{\rho(j,k) + \rho(j,k+1)} \quad (3.12)$$

$$c_4 = \frac{2}{\rho(j,k) + \rho(j,k-1)} \quad (3.13)$$

where $\rho(j, k)$ is the resistivity [ohm-m] of the node at grid coordinates j, k .

3.3.2 Iteration method

In order to solve Equation (3.9) numerically and obtain the results for electrical potential ϕ at each point on the grid, the iterative method called Successive Over-Relaxation was used (Spencer and Ware, 2009). At first, a guess is made for $\phi(j, k)$ across the whole grid, for example $\phi(j, k) = 0$ for all j, k . That guess is then used to calculate the right hand side of Equation (3.9) for each point and the new set of values for $\phi(j, k)$ is calculated using the following iteration scheme,

$$\phi_{n+1} = \omega Rhs + (1 - \omega)\phi_n \quad (3.14)$$

The multiplier ω is used to shift the eigenvalues so the iteration converges better than simple relaxation. The number ω is between 1 and 2, and when the computing region is rectangular the following equation can be used to get a reasonable good value for ω ,

$$\omega = \frac{2}{1 + \sqrt{1 - R^2}} \quad (3.15)$$

where

$$R = \frac{\left(\cos\left(\frac{\pi}{Nx}\right) + \cos\left(\frac{\pi}{Ny}\right) \right)}{2} \quad (3.16)$$

The natural Neumann boundary condition was used on the outer boundaries, i.e. $\frac{\partial \phi}{\partial n} = 0$.

3.4 RESULTS

The resistivity model was used first to study the possibility of using potential difference between only two points in a reservoir to infer at what angle a straight fracture between the points is placed. The field is 160x160 m with resistivity as 1 Ω m, and the fracture is about 60 m with resistivity 10,000 Ω m. Figure 3.2 shows the fracture (gray blocks) modeled with angle θ to the horizontal, and two wells (black blocks) modeled at points (-50,50) and (50,-50).

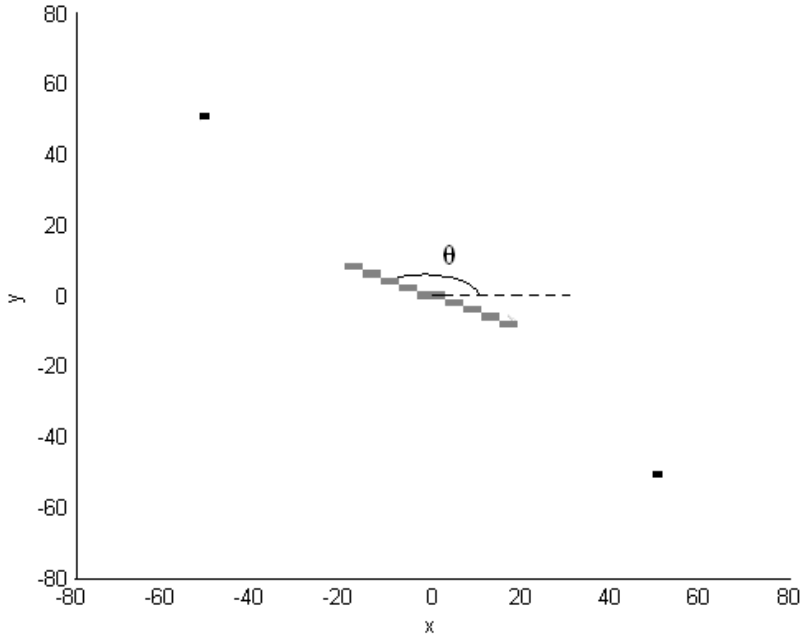


Figure 3.2: Two wells (black blocks) and a fracture (grey blocks) modeled.

A current is set equal to 1 A at the well block in the upper left corner, and as -1 A at the well block in the lower right corner, and the potential distribution is calculated for different angles, θ . The potential difference is lower for a fracture parallel to a straight line between the two wells (i.e. $\theta = 135^\circ$) than for a fracture perpendicular to that line (i.e. $\theta = 45^\circ$), since the fracture is modeled with lower conductivity than the reservoir. Only one, relatively small fracture is modeled so the difference between the two configurations is low, or 2.4112 V for $\theta = 135^\circ$ and 2.4182 V for $\theta = 45^\circ$. Figure 3.3 shows the results for various angles.

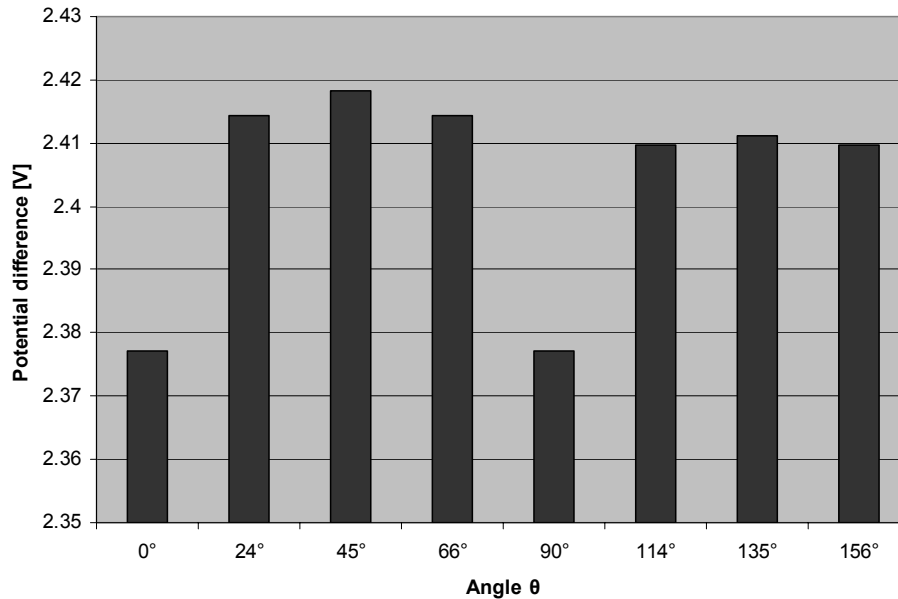


Figure 3.3: Potential difference for various well alignments.

A fracture placed with angle 0° to the horizontal gives the same potential difference as a fracture placed with angle 90° , as expected, since those fractures are symmetric to each other with respect to a straight line between the wells (see Figure 3.4). Knowing the potential difference between those two wells is therefore not enough to distinguish between those two alignments of fractures. The same goes for the other symmetric angles tested, i.e. angles $\theta = 24^\circ$ and $\theta = 66^\circ$ and angles $\theta = 114^\circ$ and $\theta = 156^\circ$.

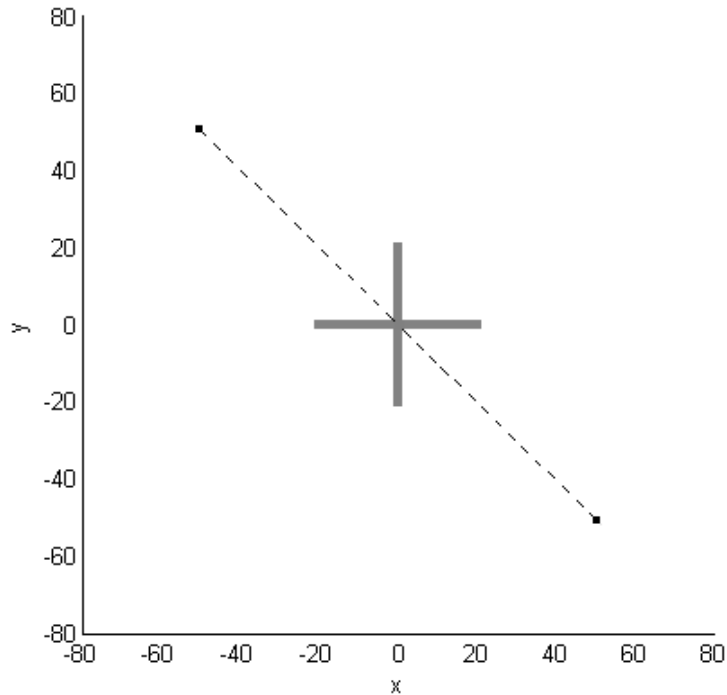


Figure 3.4: Two fractures (grey blocks) symmetric to each other with respect to a straight line (dotted line) between the wells (black blocks).

Conductive fluid was modeled as a way of enhancing the difference between fracture and rock resistivity and potential difference is measured at various times, i.e. when the fluid is at different locations, which helps in recognizing some types of fractures. For example, when a fracture is parallel to a straight line between the wells, i.e. $\theta = 135^\circ$, the conductive fluid injected makes a part of the fracture more conductive, so the potential difference between the wells is lower than before. But when the fracture is placed at $\theta = 45^\circ$, the conductive fluid behaves differently, as the fluid is located elsewhere in the field at that point of time. The potential difference between those two cases is therefore more detectable when using conductive fluid. The fluid does, however, not help in distinguishing between two fractures symmetric with respect to the straight line between the wells.

Various fracture patterns were modeled to study further whether only two wells can be used to characterize the patterns. Some variation can be seen in the potential distribution for the various patterns, which could be helpful in suggesting fracture properties. Some of the patterns have, however, the same potential differences, for example the patterns shown in Figure 3.5 and Figure 3.6.

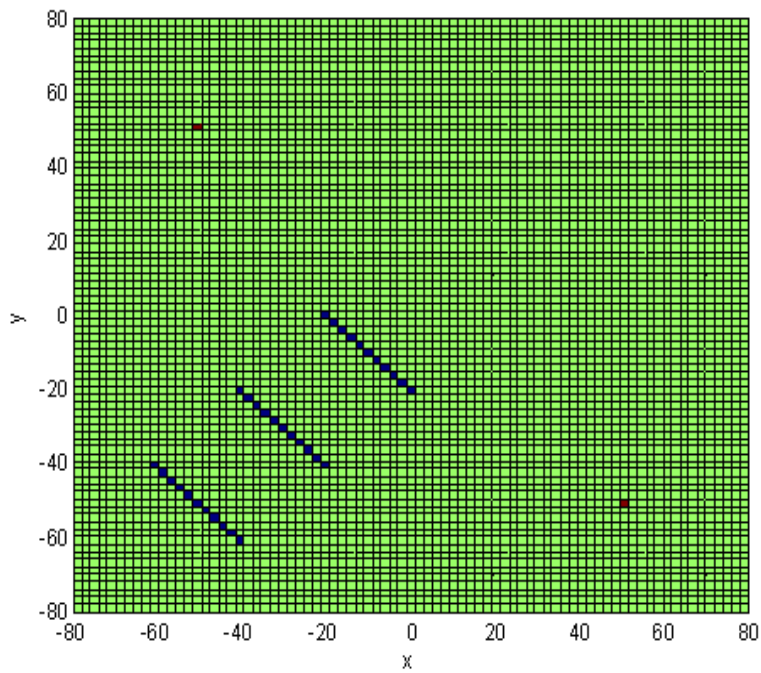


Figure 3.5: Three parallel fractures modeled with an angle 135° to the horizontal.

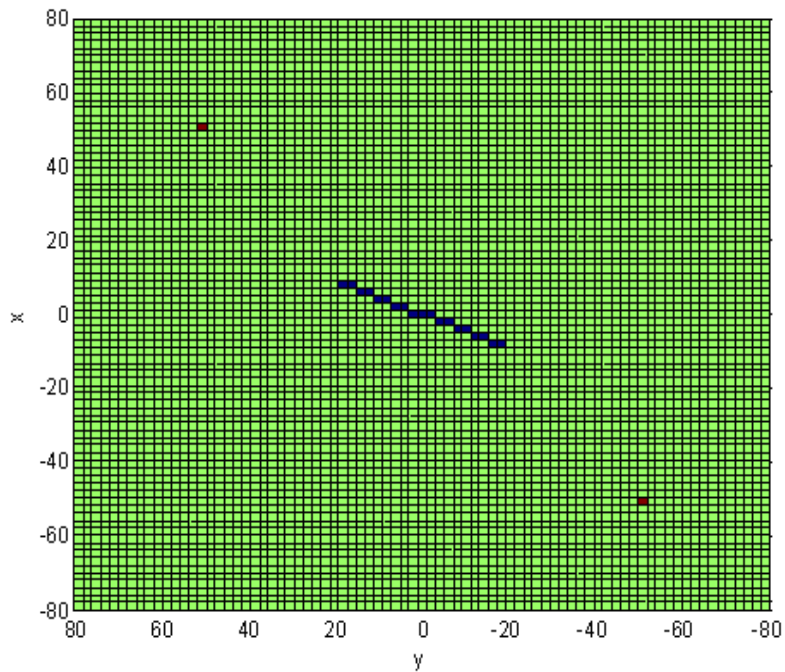


Figure 3.6: One fracture modeled with an angle 156° to the horizontal.

Those two different fracture patterns, i.e. the three parallel fractures with an angle 135° to the horizontal, shown in Figure 3.5, and the single fracture modeled with an angle 156° to the horizontal, shown in Figure 3.6, have the same potential difference between the two

wells, 2.4096 V. Therefore the difference could not be used to distinguish between those patterns. However a third well, located in the lower left corner, could be used to observe potential differences between all three wells, and thereby be used to distinguish between the patterns. There are usually only a few test wells in a geothermal reservoir, so it is important to find a way to use as few measure points as possible to characterize the fractures.

The small difference between fracture patterns is because the fractures modeled are relatively thin and short. Greater difference would probably be observable between more complex patterns, and between big and small fractures or between large and small number of fractures. If the potential difference is known for a large number of patterns, those statistics could be used to imply a fracture pattern for an unknown field, or at least be used to eliminate a number of infeasible patterns, thereby giving a better estimate of the fracture field. That way, the difference can hopefully be used to characterize the patterns to infer the fracture properties.

3.5 FUTURE WORK

One of the next steps is to use the program to look at potential fields for more realistic fracture patterns, i.e. with a larger number of fractures, and study whether the results can be used to imply a fracture pattern for a known potential difference, or at least to eliminate infeasible patterns. Another future step is to explore the benefits of using three wells instead of two and also to investigate further the possibility of using conductive fluid to enhance the difference between fracture and rock resistivity, making it easier to distinguish between the two.

Other future goals are to study the influences of temperatures on water resistivity as well as the potential changes due to fluid flowing in the fractures (streaming potential). Also, the effects of mineralization will be examined because it could either help or hinder the attempt to distinguish between rock and fractures containing minerals.

4. REFERENCES

- Alaskar, Mohammed N., Horne, R.N. and Li, Kewen (2009), “Fracture Characterization of Enhanced Geothermal Systems Using Nanoparticles,” DOE quarterly report (2009 April to June), Contract DE-FG36-08GO18192, 17-29.
- Alaskar, Mohammed N., Horne, R.N. and Li, Kewen (2009), “Fracture Characterization of Enhanced Geothermal Systems Using Nanoparticles,” DOE quarterly report (2009 July to September 2009), Contract DE-FG36-08GO18192, 17-29.
- Arnason, K.: Viðnámsmælingar í Jarðhitarannsóknnum á Íslandi, Orkustofnun, Orkuþing (2001).
- Connor, Steve. <stconnor1@gmail.com> (2010, March 11). [Personal email].
- Dey, A. and Morrison, H.F.: Resistivity Modeling for Arbitrarily Shaped Two-Dimensional Structures, Geophysical Prospecting 27, I06-I36, University of California, Berkeley, CA (1979).
- Horne, R., and Rodriguez, F., Dispersion in tracer flow in fractured geothermal systems, Proceedings of Seventh Workshop on Geothermal Reservoir Engineering, Stanford University, Stanford, CA, (1983), 103-107.
- Holder, D.S.: Electrical Impedance Tomography: Methods, History and Applications, IOP, UK (2004).
- Juliusson E. and Horne, R.N.: Fracture characterization using production and injection data, DOE quarterly report (2009 July to September), Contract DE-FG36-08GO18192, Stanford Geothermal Program, Stanford University, California, (2009a), 1-24.
- Juliusson E. and Horne, R.N.: Fracture characterization using production and injection data, DOE quarterly report (2009 October to December), Contract DE-FG36-08GO18192, Stanford Geothermal Program, Stanford University, California, (2009b), 1-24.
- Lauwerier, H.A., The transport of heat in an oil layer caused by the injection of hot fluid, Applied Scientific Research, 5, (1955) 145-150.
- MathWorks: Partial Differential Equation Toolbox 1, The MathWorks™, Inc. (2003).
- Mufti, I.R.: Finite-Difference Resistivity Modeling for Arbitrarily Shaped Two-Dimensional Structures, Geophysics, 41, (1976), 62-78.
- Ozaki, M., Kratochvil, S., Matijevic, E. (1984), J. Colloid Interface Sci., 102, 146-151.
- Shewchuk J.R.: Triangle: Engineering a 2D Quality Mesh Generator and Delaunay Triangulator, Applied Computational Geometry: Towards Geometric Engineering, 1148, Springer-Verlag, Berlin, (1996), 203-222.
- Spencer, R.L. and Ware, M.: Computational Physics 430, Partial Differential Equations, Department of Physics and Astronomy, Brigham Young University (2009).

- Stacey, R.W., Li, K. and Horne, R.N.: Electrical Impedance Tomography (EIT) Method for Saturation Determination, Proceedings, 31st Workshop on Geothermal Reservoir Engineering, Stanford University, Stanford, CA (2006).
- Suzuki, S., Caumon, G., and Caers J., Dynamic data integration for structural modeling: model screening approach using a distance-based model parameterization. *Computational Geosciences*, 12, (2008) 105-119.
- Suzuki, S., and Caers J., A Distance-based Prior Model Parameterization for Constraining Solutions of Spatial Inverse Problems, *Mathematical Geosciences*, 40, (2008), 445-469.
- Takahashi, H., Watanabe, K., and Hashida, T., Future target for geothermal development - Fractal fracture mechanics and its application to conceptual HDR reservoir design, Proceedings of Twentieth Workshop on Geothermal Reservoir Engineering, Stanford University, Stanford, CA, (1995) 167-174.
- Wang, P. and Horne, R.N.: Integrating Resistivity Data with Production Data for Improved Reservoir Modelling, SPE 59425, SPE Asia Pacific Conference, Yokohama, Japan (2000).
- Wang, Hui, et al. (2006), "Nanorice: A Hybrid Plasmonic Nanostructure," *Nano Letters*, 6.4, 827-32.
- Watanabe, K., and Hideaki T., Fractal geometry characterization of geothermal reservoir fracture networks, *Journal of Geophysical Research-Solid Earth*, 100, (1995), 521-528.